JOURNAL OF SPACECRAFT AND ROCKETS
Vol. , No. ,

Solar and Thermal Radiation Models and Flight Evaluation for IKAROS Solar Sail

Jozef van der Ha*
Deming, Washington 98244
and
Yuya Mimasu,† Yuichi Tsuda,‡ and Osamu Mori§
Japan Aerospace Exploration Agency, Sagamihara 229-8510, Japan

DOI: 10.2514/1.A33158

This paper gives a detailed evaluation of the solar and thermal radiation accelerations acting on the IKAROS spacecraft consisting of a solar sail and a central body during its operational mission from June to December 2010. In particular, the predicted temperatures are compared with actual in-flight measurements on the sail membrane and on the body. The results show good correspondences in most cases, but a few appreciable deviations have been observed as well. The simulation results indicate that the magnitude of the thermal radiation perturbations on the solar sail trajectory is below 1% of those induced by the solar radiation. The accelerations caused by the thermal radiation turn out to be insignificant because their magnitudes are within the range of uncertainty of the accelerations induced by the solar radiation forces.

Nomenclature

A = surface area, m^2
$\boldsymbol{a}$ = acceleration vector, m/s^2
C_{SRP} = vector, μm/s^2
c = velocity of light, m/s
d = solar distance, astronomical unit (AU)
F, G = auxiliary functions
f, g = auxiliary functions, m/s^2
I = intensity of radiation, W/(m^2 · sr)
m = mass, kg
$\boldsymbol{n}$ = surface-normal unit vector
Q = heat, W
q = heat flux, W/m^2
r, s = reflectivity parameters
S = 1366.1 W/m^2, mean solar constant at 1 AU
$\boldsymbol{s}$ = spacecraft-to-sun unit vector
T = temperature, K or °C
$\boldsymbol{t}$ = unit vector normal to $\boldsymbol{s}$
α = absorptivity, $0 < \alpha < 1$
ε = emissivity, $0 < \varepsilon < 1$
ϑ = sun incidence angle
κ = emissivity parameter
ρ = reflectivity coefficient, $0 < \rho < 1$
σ = 5.67×10^{-8} W/(m^2 · K^4), Stefan–Boltzmann constant

Subscripts

bot = bottom
con = converted
d = diffusely reflective
dis = dissipated
f = front
in = incident
j = index of surface element
out = outgoing
r = rear
s = specularly reflective

I. Introduction

THE solar-sail probe IKAROS (from "interplanetary kite-craft accelerated by radiation of the sun") was designed and implemented by the Japan Aerospace Exploration Agency (JAXA) [1,2]. IKAROS was launched together with JAXA's Venus Climate Orbiter Akatsuki by JAXA's H-IIA launch vehicle on 21 May 2010. Both satellites were injected into direct transfer trajectories toward Venus. Thus, IKAROS became the very first solar sail ever to actually fly an interplanetary voyage. Thereby, it confirmed the feasibility of the propulsive acceleration induced by the solar radiation pressure (SRP). Furthermore, IKAROS demonstrated several new technologies, for instance the full deployment of the sail membrane during its interplanetary cruise, the thin-film solar power generation, and the attitude control by modification of the sail's surface reflectivity.

A crucial aspect of solar sailing is the precise modeling of the force induced by the SRP in support of its navigation objectives. Because the SRP force vector varies with the solar sail's attitude orientation, a detailed SRP torque model is essential for IKAROS. The unique estimation and modeling of IKAROS with regard to orbit and attitude dynamics and their cross-couplings have been addressed in detail in earlier papers [3–8]. Furthermore, extensive information on IKAROS in-flight operations performances is available in the literature [6].

The IKAROS spacecraft consists of a central body equipped with a large, thin solar sail membrane. It is slowly spinning at 1 to 2 rpm, and so the sail is kept extended by the centrifugal force. A realistic in-flight dynamical modeling [7] of the sail is very complicated because the thin membrane is nonflat due to wrinkling and nonuniform in terms of optical parameters. Interestingly, the common parameters in the force and torque models can be estimated [8] in-flight from the radiometric tracking measurements.

Another small force is generated by the thermal radiation pressure (TRP) on the IKAROS sail membrane and on its body surfaces. TRP is caused by the recoil of reemitted thermal radiation. The induced force is governed by the temperatures of the radiating external spacecraft surfaces and on the attitude orientation. The TRP effects are usually overlooked, but they may be incorporated, knowingly or unknowingly, in SRP-scale factors that compensate for the differences of the observed and estimated SRP forces [9].

Presented as Paper 2014-0244 at the 24th AAS/AIAA Space Flight Mechanics Meeting, Santa Fe, NM, 26–30 January 2014; received 15 September 2014; revision received 7 January 2015; accepted for publication 19 February 2015;

*Consultant, 5808 Bell Creek Road; jvdha@aol.com. Senior Member AIAA.

[†] Engineer; mimasu.yuya@jaxa.jp.

[‡] Assistant Professor; tsuda.yuichi@jaxa.jp.

[§] Assistant Professor; mori.osamu@jaxa.jp.

Table 1 Overview of principal solar sail technology devices

Acronym	Device	Description
FSA	Flexible solar array	Thin-film flexible solar-cell power generator (300 W at 1 AU) using incident sunlight
RCD	Reflectance control device	Steering device for attitude control of sail using liquid crystals and voltage regulator
ALDN	Arrayed large-area dust detector	Polyvinylidene fluoride (PVDF)-based film sensor of 0.5 m^2 area for detecting particles impacting the sail

The model presented here predicts the TRP-induced accelerations on the basis of the heliocentric distance and the thermo-optical properties of the IKAROS spacecraft (i.e., sail membrane as well as body) surfaces. Unlike SRP effects, the thermal forces depend on the temperatures of the surface elements and vary with their attitude orientations relative to the sun direction. Although smaller in magnitude than the SRP forces, the TRP force may well act in a direction that is significantly different from the SRP force direction [10–16].

This paper summarizes and evaluates the models and results of the accelerations induced by the SRP and TRP effects acting on the IKAROS solar sail membrane plus body surfaces during its half-year deep-space mission. Furthermore, the temperatures predicted by the thermal models are compared with the actually observed in-flight values (for the sail as well as body surfaces).

II. Configuration of IKAROS Sail Membrane and Body

The IKAROS sail membrane measures $14 \times 14\ m^2$ with a tip-to-tip length of about 20 m. It is deployed from the cylindrical hub at the center of the body; see Figs. 1a and 1b. The membrane consists of polyimide-evaporated 80 nm aluminum of 7.5 μm thickness. It has high thermal, mechanical, and chemical resistance properties and extremely low mass. Thus, it is a critical enabler for solar sail manufacturing. The incident sunlight on the reflective aluminum front of the membrane generates the thrust force.

Various technology devices are placed on the sail membrane; see Fig. 2 and Table 1. A principal device is the flexible solar arrays (FSAs), which are thin-film solar-cell power generators from incident sunlight. Another is the reflectivity control device (RCD), which is a novel steering device for attitude control purposes. It is made of a liquid crystal where the ratio of specular and diffuse reflectivity may be modified by varying the applied voltage. In this manner, differences may be induced in the effective solar radiation force acting on different RCD surface elements. Mori et al. [2] and Tsuda et al. [6] give more details on the IKAROS design and operations aspects.

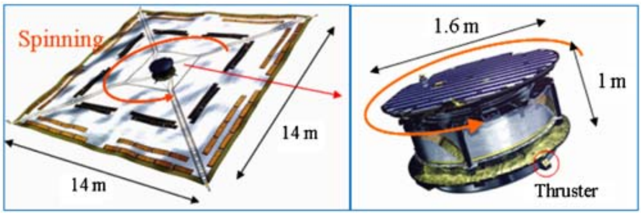

Fig. 1 Representations of a) IKAROS square solar sail membrane, and b) IKAROS body.

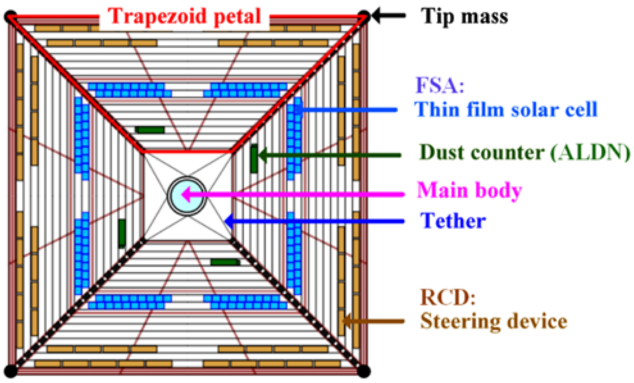

Fig. 2 Configuration of IKAROS solar sail and devices.

III. Solar Radiation Pressure Model

The solar and thermal radiation forces acting on IKAROS depend on several parameters such as the solar distance d, the effective surface area A, the solar incidence angle ϑ (between the surface normal and the sun direction), and the thermo-optical reflective properties of the surface materials. For convenience, the solar sail surface is taken perfectly flat. A nonflat spin-type solar sail surface has a 4% lower effective thrust force compared to the ideal flat sail. This is because of the lower effective sail area and a lower effective reflectivity; see Sec. 4.2 in [6].

The IKAROS solar sail membrane in Fig. 2 contains seven different surface elements that are always exposed to the sun. Also, the top body surface ($j = 8$) is always exposed. On the other hand, the rear body surface is never exposed to the sun during its nominal mission. It should be noted that the thermo-optical parameters vary considerably among the different surface elements of the membrane. The total sun-exposed flat surface area of sail plus body is $A_{\mathrm{SRP}} = 183.54\ \mathrm{m}^2$, with the body top surface contributing close to 1% of the total surface area.

Here, we assume that the orientations of the body top surface and the sail with respect to the sun are identical as illustrated in Fig. 1. In reality, however, this is not exactly true, as indicated by the discrepancies in the IKAROS body orientation observed by its attitude sensors and the estimated sail attitude orientation derived from the radiometric measurements; see [8].

The acceleration induced by the solar radiation pressure acting on an arbitrary flat surface with effective area A_{SRP} can be expressed in terms of the SRP coefficient C_{SRP}; see [10]:

$$C_{\mathrm{SRP}} = \frac{1}{d^2}\frac{S}{c}\frac{A_{\mathrm{SRP}}}{m}\ \mathrm{m/s^2} \tag{1}$$

When using IKAROS sail plus body values $A_{\mathrm{SRP}} = 183.54\ \mathrm{m}^2$, $m = 307$ kg, we find $C_{\mathrm{SRP}} = 2.724\ \mu\mathrm{m/s^2}$ at $d = 1$ AU.

The incident solar radiation flux is broken up in its fractions in accordance with the surface's optical reflective properties (while disregarding highly transmissive surfaces):

$$\alpha + \rho_s + \rho_d = 1 \Rightarrow \rho = \rho_s + \rho_d = 1 - \alpha \tag{2}$$

The SRP-induced acceleration $\boldsymbol{a}_{\mathrm{SRP}}$ may be written in terms of its components along the instantaneous sun direction $\boldsymbol{s}$ and along the surface normal $\boldsymbol{n}$; see Fig. 3:

$$\boldsymbol{a}_{\mathrm{SRP}} = f\boldsymbol{s} + g\boldsymbol{n} \tag{3}$$

with f and g defined as follows; see Eqs. (7) and (8) in [10]:

$$\begin{pmatrix} f \\ g \end{pmatrix} = -C_{\mathrm{SRP}} \cos\vartheta \begin{pmatrix} 1 - \rho_s \\ 2\rho_d/3 + 2\rho_s \cos\vartheta \end{pmatrix} \tag{4}$$

If the sun direction is normal to the surface (i.e., when $\vartheta = 0$ deg), the ratio $|\boldsymbol{a}_{\mathrm{SRP}}|/C_{\mathrm{SRP}}$ lies within the interval [1,2] because the reflectivity parameters ρ_s and ρ_d are bounded by $0 < \rho_s + \rho_d < 1$; see [11].

The SRP-induced acceleration of IKAROS follows from Eqs. (3) and (4) by adding all contributions of the sun-exposed surface

Table 2 Area-weighted thermo-optical parameters of sail membrane plus body top

	SRP parameters			TRP parameters	
Sun-exposed area, m^2	ρ_s	ρ_d	α	ε_f	ε_r
183.54	0.723	0.117	0.160	0.216	0.573

elements A_j $(j = 1, 2, \ldots, 8)$ and assigning a specific SRP coefficient $C_{\mathrm{SRP},j}$ to each surface element A_j, similar to Eq. (1) but using A_j instead of the total area A_{SRP}:

$$\boldsymbol{a}_{\mathrm{SRP}} = \sum_{j=1}^{8} \{f_j \boldsymbol{s} + g_j \boldsymbol{n}_j\} \tag{5}$$

with f_j and g_j defined as in Eq. (4) but in terms of $C_{\mathrm{SRP},j}$ $(j = 1, 2, \ldots, 8)$ instead of C_{SRP}.

Here we assume that the surface elements of the IKAROS sail membrane remain perfectly flat and aligned with the top body surface at all times. Thus, the normal vectors of all sail surface elements and the body top surface will be taken identical: $\boldsymbol{n}_j = \boldsymbol{n}$ $(j = 1, 2, \ldots, 8)$. Furthermore, all surface elements now have the same solar incidence angle, i.e., $\vartheta_j = \vartheta$ (for $j = 1, 2, \ldots, 8$), and Eq. (5) can be written as

$$\boldsymbol{a}_{\mathrm{SRP}} = -\cos\,\vartheta \sum_{j=1}^{8} C_{\mathrm{SRP},j}\{(1 - \rho_{s,j})\boldsymbol{s} + 2(\rho_{d,j}/3 + \rho_{s,j}\cos\,\vartheta)\boldsymbol{n}\}$$

$$= -C_{\mathrm{SRP}}\cos\,\vartheta\{\langle 1 - \rho_s\rangle \boldsymbol{s} + 2\langle \rho_d/3 + \rho_s \cos\,\vartheta\rangle \boldsymbol{n}\} \tag{6}$$

where $\langle x\rangle$ designates the area-weighted average of x appearing within the brackets:

$$\langle x\rangle = \frac{1}{A_{\mathrm{SRP}}} \sum_{j=1}^{8} (A_j x_j) \tag{7}$$

Table 2 summarizes the area-weighted averages of the thermo-optical parameters of the sun-exposed area that includes the seven sail membrane elements as well as the body top surface $(j = 8)$.

When using the reference input values $\vartheta = 0$ deg and $d = 1$ AU, we obtain the following explicit numerical reference acceleration from Eq. (6):

$$\boldsymbol{a}_{\mathrm{SRP,ref}} = -a_{\mathrm{ref}}\boldsymbol{n} \tag{8a}$$

with

$$a_{\mathrm{ref}} = C_{\mathrm{SRP}}\langle 1 + 2\rho_d/3 + \rho_s\rangle = 4.910\ \mu\mathrm{m/s}^2 \tag{8b}$$

The estimated reference acceleration derived from in-flight observations (see Fig. 2 in [8]) is about 12% smaller than the predicted value in Eq. (8b). This difference is mainly due to the change in effective area of the three-dimensional mildly conical shape of the deployed spinning membrane compared to a perfectly flat sail. Also, wrinkling of the membrane surface and variations in its reflectivity properties under different solar aspect angles and temperatures as well as potential degradation of the sail over its lifetime play a role; see [6,7].

For navigation purposes, the SRP acceleration vector is usually expressed in its components along the sun vector and normal to the sun direction. Therefore, the sail's normal vector $\boldsymbol{n}$ must be expanded in components along the sun vector $\boldsymbol{s}$ and along the unit vector $\boldsymbol{t}$. The latter vector lies within the plane defined by the unit vectors $\boldsymbol{n}$ and $\boldsymbol{s}$ and points normal to $\boldsymbol{s}$, as shown in Fig. 3:

$$\boldsymbol{n} = \cos\,\vartheta\boldsymbol{s} + \sin\,\vartheta\boldsymbol{t} \tag{9}$$

Afterward, the vector $\boldsymbol{t}$ may be expanded in components along any other two reference axes within the plane normal to the sun vector.

Equation (6) can now be expressed as follows:

$$\boldsymbol{a}_{\mathrm{SRP}} = -C_{\mathrm{SRP}}\{F\boldsymbol{s} + G\boldsymbol{t}\} \tag{10}$$

with

$$F = \cos\,\vartheta\langle 1 - \rho_s\rangle + 2\cos^2\vartheta\langle \rho_d/3 + \rho_s\cos\,\vartheta\rangle \tag{11a}$$

$$G = 2\cos\,\vartheta\,\sin\,\vartheta\langle \rho_d/3 + \rho_s\cos\,\vartheta\rangle \tag{11b}$$

By using straightforward algebraic manipulations, Eqs. (11a) and (11b) may be written in the form of a truncated Fourier series:

$$F = r + (1 + s)\cos\,\vartheta + r\cos(2\vartheta) + s\cos(3\vartheta) \tag{12a}$$

$$G = s\sin\,\vartheta + r\sin(2\vartheta) + s\sin(3\vartheta) \tag{12b}$$

with

$$r = \langle \rho_d\rangle/3 \tag{13a}$$

$$s = \langle \rho_s\rangle/2 \tag{13b}$$

As expected, Eqs. (12) and (13) contain only two independent coefficients (i.e., r and s), which are proportional to the area-weighted averages of the diffuse and specular reflectivity coefficients, respectively.

IV. Thermal Radiation Pressure Model

A. Model for Sail Surface Elements

We make the realistic assumption that, during normal-mode operations, the sail is in a steady-state thermal equilibrium. Therefore, all incident solar radiation energy that is absorbed by the sail membrane must also be reradiated into space. The reemitted heat fluxes, the surface temperatures, and the induced TRP accelerations can all be established from a straightforward steady-state thermal balance.

Also, we assume that the heat transfer between the individual surface elements is negligible in comparison with the conductive front-to-rear heat transfer through the 7.5-μm-thin sail membrane. In this situation, each surface element may well have a different temperature and may be considered to be largely isolated from neighboring elements. On the other hand, the temperatures on the front and rear of each sail element are expected to be identical because of the extreme thinness of the sail.

In the next section, we introduce, for comparison, a virtual sail that has the (uniform) weighted average thermal properties of the actual membrane. Thus, the incident solar heat is absorbed and reemitted evenly over the sail surface, and the temperature of the virtual sail will be identical throughout.

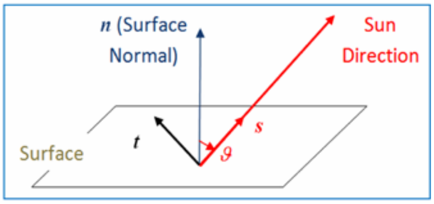

Fig. 3 Sun angle ϑ and unit vectors $\boldsymbol{n}$, $\boldsymbol{s}$, and $\boldsymbol{t}$ relative to flat surface.

In both of these models, the incoming and outgoing heat fluxes can be described as follows. First, we have q_{in}, which is the fraction of incident solar radiation flux that is absorbed by the front side of a surface element. Second, $q_{f,\text{out}}$ is the thermal radiation flux that is reemitted by the front side of a surface element. Finally, $q_{r,\text{out}}$ represents the thermal radiation reemitted flux from the rear side of a surface element.

Figure 4a illustrates the balance of the incident and reemitted heat fluxes for an arbitrary surface element A. Figure 4b shows the acceleration $\boldsymbol{a}_{\text{TRP}}$ resulting from the diffuse thermal reemission by the front side of the surface A. In the thermal balance case illustrated in Fig. 4a, the thermal emission on the rear side will create a similar but opposite acceleration. The magnitudes of the front and rear accelerations are usually different due to unequal front and rear emissivity values.

The thermal heat balance of surface A_j under a solar incidence angle ϑ with $0 < \vartheta < 90$ deg is

$$q_{\text{in},j} = \alpha_{f,j}(S/d^2)\cos\vartheta = q_{f,\text{out},j} + q_{r,\text{out},j} \qquad (j = 1, 2, \ldots, 7) \tag{14}$$

where $q_{\text{in},j}$ is the solar flux absorbed by the front side of A_j. The heat fluxes emitted by the surface's front and rear sides are determined by the front and rear temperatures $T_{f,j}$ and $T_{r,j}$ and by the surface thermal emissivities $\varepsilon_{f,j}$ and $\varepsilon_{r,j}$ in accordance with the Stefan–Boltzmann law.

Under the assumed perfect heat conductivity through the thin membrane, the front and rear temperatures of the surface elements will be identical (i.e., $T_{f,j} = T_{r,j} = T_j$), and so we have

$$q_{f,\text{out},j} = \varepsilon_{f,j}\sigma T_j^4 \tag{15a}$$

$$q_{r,\text{out},j} = \varepsilon_{r,j}\sigma T_j^4 \tag{15b}$$

By combining Eqs. (14) and (15) we obtain the resulting temperature T_j for each surface element A_j:

$$T_j = \left\{\frac{q_{\text{in},j}}{(\varepsilon_f + \varepsilon_r)_j\sigma}\right\}^{1/4} = \left\{\frac{\alpha_{f,j}S\cos\vartheta}{(\varepsilon_f + \varepsilon_r)_j\sigma d^2}\right\}^{1/4} \tag{16}$$

The accelerations due to the diffuse thermal radiation emissions on the front and rear of the surface A_j follow from Eqs. (15) by the recoil principle similarly as in the SRP acceleration of Eq. (1):

$$\boldsymbol{a}_{\text{TRP},f,j} = -\frac{2}{3}\frac{q_{f,\text{out},j}}{c}\frac{A_j}{m}\boldsymbol{n} \tag{17a}$$

$$\boldsymbol{a}_{\text{TRP},r,j} = +\frac{2}{3}\frac{q_{r,\text{out},j}}{c}\frac{A_j}{m}\boldsymbol{n} \tag{17b}$$

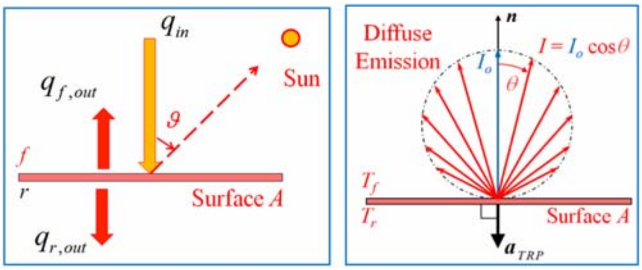

Fig. 4 Representations of a) thermal balance of surface A, and b) diffuse emission and TRP acceleration.

The factor $2/3$ originates from Lambert's cosine-law emission profile shown in Fig. 4b. It may be noted that the acceleration that is induced by the absorbed fraction $q_{\text{in},j}$ of the incident solar radiation power in Eq. (14) has already been incorporated in the SRP contribution; see Eqs. (1–6).

The net acceleration due to the thermal radiation emitted by both sides of the surface element A_j follows by adding the results of Eqs. (17a) and (17b). When substituting the expressions in Eq. (15), the net acceleration can be written in terms of the temperature T_j:

$$\boldsymbol{a}_{\text{TRP},j} = -\frac{2}{3}(\varepsilon_f - \varepsilon_r)_j\frac{\sigma T_j^4}{c}\frac{A_j}{m}\boldsymbol{n} \tag{18}$$

The temperature T_j in Eq. (18) may be replaced by the radiation $q_{\text{in},j}$ with the help of Eqs. (14) and (15):

$$\boldsymbol{a}_{\text{TRP},j} = -\frac{2}{3}\left(\frac{\varepsilon_f - \varepsilon_r}{\varepsilon_f + \varepsilon_r}\right)_j\frac{q_{\text{in},j}}{c}\frac{A_j}{m}\boldsymbol{n} \tag{19}$$

When recalling Eq. (1), we obtain the final expression for the TRP-induced acceleration:

$$\boldsymbol{a}_{\text{TRP},j} = -\frac{2}{3}(\alpha_f\kappa C_{\text{SRP}})_j\cos\vartheta\boldsymbol{n} \qquad (j = 1, 2, \ldots, 7) \tag{20}$$

with the emissivity parameter κ_j defined by

$$\kappa = (\varepsilon_f - \varepsilon_r)/(\varepsilon_f + \varepsilon_r) \tag{21}$$

The C_{SRP} term in Eq. (20) indicates the close relationship between the TRP and SRP phenomena.

Finally, the total TRP-induced acceleration induced by the seven individual sail elements equals the sum of their individual contributions in Eq. (20).

B. Model for Uniform Virtual Sail

Here, we study the uniform virtual sail that is defined by the weighted average properties of the IKAROS sail thermal parameters. The incident solar power on the total sail area A_{sail} (without the top body surface) of 181.77 m^2 is Q_{in}, and Eq. (14) gives

$$Q_{\text{in}} = \sum_{j=1}^{7}(A_j q_{\text{in},j}) = \left(\frac{S}{d^2}\right)\cos\vartheta\sum_{j=1}^{7}(A_j\alpha_{f,j}) \tag{22}$$

This equation may be rewritten as

$$q_{\text{in}} = \frac{Q_{\text{in}}}{A_{\text{sail}}} = \langle\alpha_f\rangle\left(\frac{S}{d^2}\right)\cos\vartheta \tag{23}$$

where $\langle\alpha_f\rangle$ is the area-weighted average of the seven front surface absorptivities $\alpha_{f,j}$:

$$\langle\alpha_f\rangle = \frac{1}{A_{\text{sail}}}\left\{\sum_{j=1}^{7}(A_j\alpha_{f,j})\right\} \tag{24}$$

Similarly, the total power reemitted by the sail is denoted by Q_{out}, and Eq. (15) yields

$$Q_{\text{out}} = \sum_{j=1}^{7}A_j(q_{f,\text{out}} + q_{r,\text{out}})_j = \sigma\sum_{j=1}^{7}\{A_j(\varepsilon_f + \varepsilon_r)_j T_j^4\} \tag{25}$$

This result may be written as

$$q_{\text{out}} = \frac{Q_{\text{out}}}{A_{\text{sail}}} = \frac{\sigma}{A_{\text{sail}}}\sum_{j=1}^{7}\{A_j(\varepsilon_f + \varepsilon_r)_j T_j^4\} \tag{26}$$

Now, we introduce the virtual sail with the weighted averages of the absorptivity and the (front and rear) emissivity parameters of the IKAROS sail. These properties are assumed to hold uniformly over the total sail surface. As a consequence, its temperature remains constant over the sail surface (and will be identical on the front and rear sides as well). Therefore, the resulting sail temperature T_{sail} can be separated from the summations in Eqs. (25) and (26) and follows from the heat balance condition:

$$q_{\text{in}} = q_{\text{out}} = \langle \varepsilon_f + \varepsilon_r \rangle \sigma T_{\text{sail}}^4 \tag{27a}$$

and

$$T_{\text{sail}} = \left\{ \frac{\langle \alpha_f \rangle}{\langle \varepsilon_f + \varepsilon_r \rangle} \frac{S \cos \vartheta}{\sigma d^2} \right\}^{1/4} \tag{27b}$$

where the area-weighted average $\langle \varepsilon_f + \varepsilon_r \rangle$ is defined similarly as in Eq. (24).

Finally, the accelerations of the virtual sail can be calculated as in Eqs. (17–21) but in terms of the area-weighted averaged parameters. The result will be nonzero as long as $\langle \varepsilon_f \rangle \neq \langle \varepsilon_r \rangle$.

C. Model for Body Surfaces

Figure 5a provides a visualization of the IKAROS body configuration. It also shows the incident solar radiation, which is the only external heat source. The front of the top deck is covered by solar cells and optical specular reflectors and is directly exposed to the sun. The central cylindrical hub and the upper surface of the lower deck may also be exposed, at least partially, to the solar radiation, as indicated in Fig. 5a. These exterior surfaces are covered by multilayer insulation (MLI) sheets. The outer MLI layers may be heated by the solar radiation to an extent that depends on the solar aspect angle. Because of the effective MLI insulation, no appreciable heat flux is expected to enter the body's interior.

The top deck is isolated from the cylindrical central hub, which contains the inner deck, where many of the IKAROS subsystem units are located. Other units are placed on the inside of the lower deck. Essentially all power that is dissipated by the units is transferred (i.e., conducted and radiated) to the lower deck. This deck is covered by black paint (as well as optical reflectors) on its exterior bottom to facilitate the radiation of the excess heat into space.

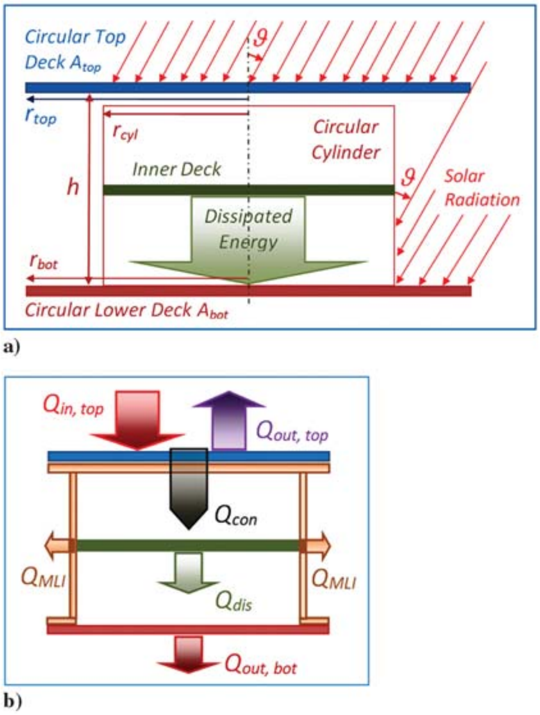

Fig. 5 Representations of a) IKAROS body configuration and heat fluxes, and b) steady-state heat balance.

Figure 5b shows the specific heat inputs and outputs that play a role in the body's heat balance. There are two conditions that must be met to guarantee the body's steady-state thermal balance. First, we consider the heat balance of the top deck. The solar power that is absorbed through the solar cells is denoted by $Q_{\text{in,top}}$. A fraction of this energy is converted [12] into electrical power (i.e., Q_{con}) and consumed by the spacecraft units on the body's inner and lower decks. The remaining part (i.e., $Q_{\text{out,top}}$) is reemitted into space. In total, we have the following condition:

$$Q_{\text{in,top}} = Q_{\text{con}} + Q_{\text{out,top}} \tag{28}$$

Second, we consider the heat balance of the exchanges that take place in the central hub and the lower deck. The converted power Q_{con} is dissipated inside the central hub and becomes waste heat (i.e., $Q_{\text{con}} = Q_{\text{dis}}$). This heat is emitted into space through the lower deck (i.e., $Q_{\text{out,bot}}$), but a small fraction Q_{MLI} may be transferred through the exterior MLI sheets, and so we have

$$Q_{\text{con}} = Q_{\text{dis}} = Q_{\text{out,bot}} + Q_{\text{MLI}} \tag{29}$$

Information on the converted power is available in the IKAROS housekeeping data, and so Q_{con} is known very accurately throughout the mission. From earlier work [10], we know that about 5 W/m^2 passes through the MLI from a spacecraft interior at 20°C into space at 3 K. Thus, the value of Q_{MLI} can readily be calculated from the geometrical properties of the body configuration shown in Fig. 5a.

The input and reemitted power sources for the top and bottom surfaces are now

$$Q_{\text{in,top}} = \alpha_{\text{top}} A_{\text{top}} (S/d^2) \cos \vartheta \tag{30a}$$

$$Q_{\text{out,top}} = \sigma \varepsilon_{\text{top}} A_{\text{top}} T_{\text{top}}^4 \tag{30b}$$

$$Q_{\text{out,bot}} = \sigma \varepsilon_{\text{bot}} A_{\text{bot}} T_{\text{bot}}^4 \tag{30c}$$

The results in Eqs. (30b) and (30c) are based on the Stefan–Boltzmann law.

The incident and emitted heat fluxes of the top and bottom surfaces are $q_j = Q_j / A_j$, where j refers to the top and bottom surfaces in Eqs. (30). The corresponding temperatures can now be derived from the known power sources in Eqs. (28) and (29):

$$T_{\text{top}} = \left\{ \frac{Q_{\text{in,top}} - Q_{\text{con}}}{\sigma \varepsilon_{\text{top}} A_{\text{top}}} \right\}^{1/4} \tag{31a}$$

$$T_{\text{bot}} = \left\{ \frac{Q_{\text{con}} - Q_{\text{MLI}}}{\sigma \varepsilon_{\text{bot}} A_{\text{bot}}} \right\}^{1/4} \tag{31b}$$

The MLI-covered cylindrical side surface does not generate a net acceleration on the body because its surface temperature is essentially uniform under the spin motion. The TRP-induced accelerations that originate from the body's top and bottom surfaces follow from Eq. (31) in a way similar to what was done for the sail in Eqs. (17) and (18):

$$\boldsymbol{a}_{\text{TRP,body}} = -\frac{2}{3} \frac{1}{mc} (Q_{\text{out,top}} - Q_{\text{out,bot}}) \boldsymbol{n} \tag{32a}$$

or

$$\boldsymbol{a}_{\mathrm{TRP,body}} = -\frac{2}{3}\frac{\sigma}{mc}\{(\varepsilon A T^4)_{\mathrm{top}} - (\varepsilon A T^4)_{\mathrm{bot}}\}\boldsymbol{n} \tag{32b}$$

In fact, the areas of the top and bottom surfaces may be taken as identical (i.e., $A_{\mathrm{bot}} = A_{\mathrm{top}}$). The result in Eq. (32b) provides the body's acceleration expressed in terms of the in-flight temperature measurements.

Alternatively, if no in-flight temperature measurements are available, we may employ the result in Eq. (32a). The heat balances in Eqs. (28) and (29) may then be used to express the heat terms in Eq. (32a) in known or predicted quantities:

$$Q_{\mathrm{out,top}} = Q_{\mathrm{in,top}} - Q_{\mathrm{con}} \tag{33a}$$

$$Q_{\mathrm{out,bot}} = Q_{\mathrm{con}} - Q_{\mathrm{MLI}} \tag{33b}$$

V. Discussion of Results

A. Solar Radiation Accelerations for Sail Plus Body Top

Figures 6a and 6b show the solar distance of IKAROS in astronomical units and the corresponding solar radiation pressure parameter C_{SRP} in units of micrometers per second squared, respectively, during the half-year IKAROS mission phase. Figure 7 shows the evolution of the solar aspect angle ϑ in degrees and its linear trend line over the same interval.

Figure 8 shows the predicted SRP-induced accelerations, in units of micrometers per second squared, in terms of their along-sun and cross-sun components. Here, along-sun refers to the spacecraft–sun direction and cross-sun stands for a direction normal to the spacecraft–sun line. The along-sun acceleration component in Fig. 8 displays a wide range of fluctuations during the mission. These are due to the variations in solar distance and solar aspect angle, as indicated in Figs. 6 and 7.

Table 3 summarizes the predicted SRP acceleration over the mission. The ratio between the acceleration components varies widely, for instance from 46 to 16% during September/October.

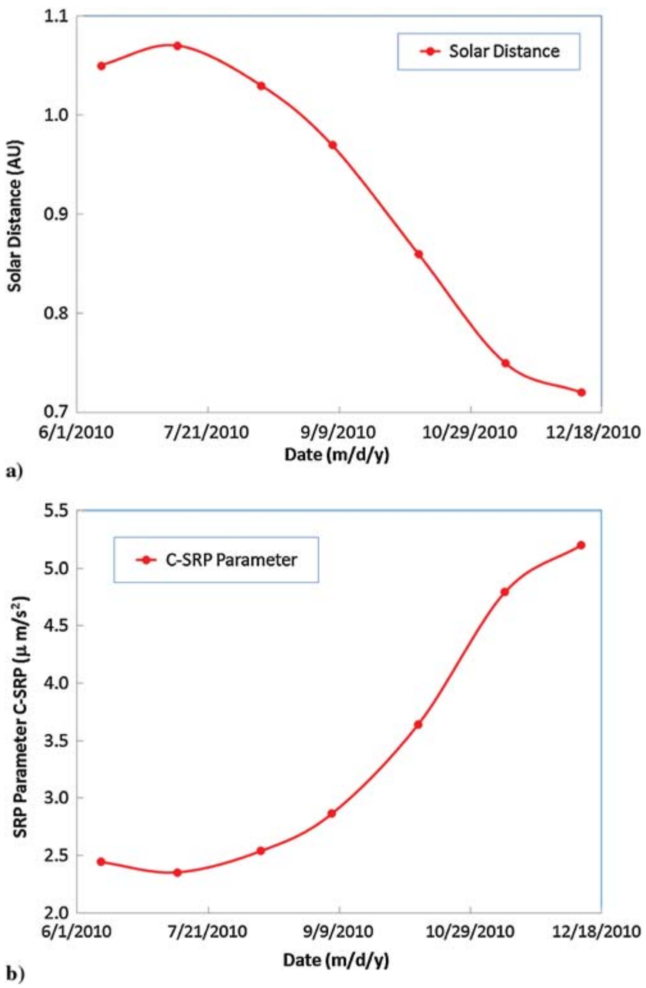

Fig. 6 Representations of a) IKAROS solar distance d during the mission, and b) IKAROS C_{SRP} parameter during the mission.

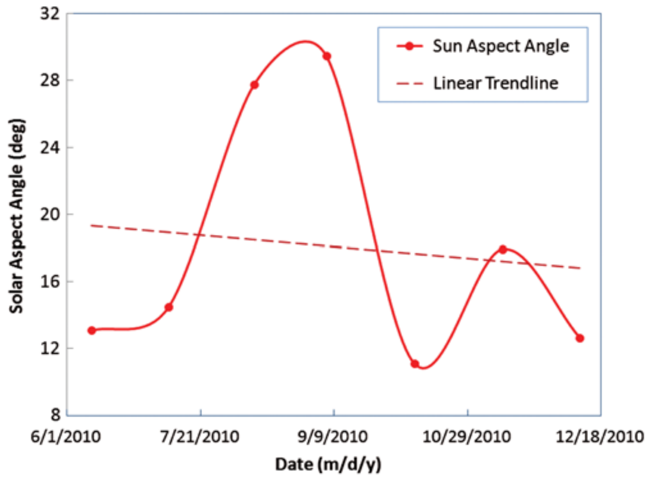

Fig. 7 IKAROS solar aspect angle ϑ during the mission.

B. Measured and Predicted Sail Temperatures

Figure 9a shows the locations of the eight thermistors on the FSAs, which carry the thin-film solar cells. The dashed lines in Fig. 9b illustrate the evolutions of the associated eight FSA temperature measurements over the half-year mission. The solid curve in Fig. 9b shows the averages of these eight measured temperatures. The solid curve in Fig. 9b gives the predicted temperatures based on Eq. (16) and the prelaunch FSA thermo-optical parameters. The two solid curves show the same qualitative trend, but the differences between the predicted and measured temperatures are fairly large (i.e., almost 9°C in average).

It is of interest to note that the predictions and measurements can effectively be reconciled by increasing the FSA absorptivity by 9.65%. Alternatively, this may also be achieved by decreasing the sum of the FSA front and rear emissivity values (i.e., $\varepsilon_f + \varepsilon_r$) by 8.8%. Therefore, it is likely that one or both of these input parameters contain bias errors up to the maximum percentage levels.

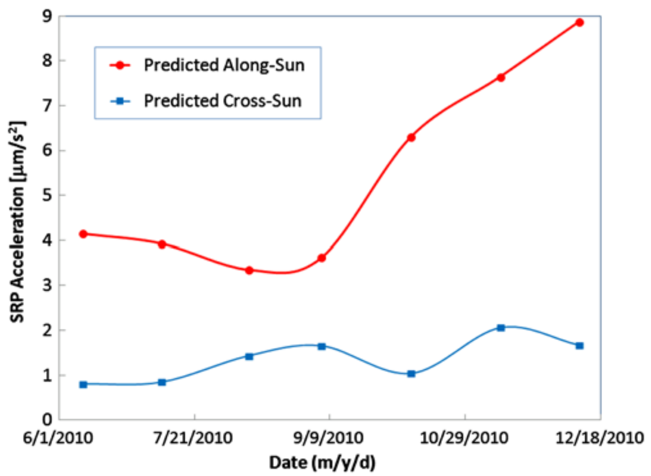

Fig. 8 Predicted IKAROS SRP acceleration components during the mission.

Table 3 Summary of IKAROS solar radiation pressure accelerations

			Accelerations, $\mu m/s^2$					
Date[a]	Sun angle, deg	Distance, AU	C_{SRP}	f_{SRP}	g_{SRP}	Along-sun	Cross-sun	Cross/along, %
6/10/2010	13.09	1.05	2.474	0.669	3.578	4.154	0.810	19.5
7/9/2010	14.49	1.07	2.382	0.640	3.406	3.938	0.852	21.6
8/10/2010	27.75	1.03	2.571	0.631	3.086	3.363	1.437	42.7
9/6/2010	29.49	0.97	2.898	0.700	3.370	3.633	1.659	45.7
10/9/2010	11.13	0.86	3.687	1.004	5.411	6.313	1.044	16.5
11/11/2010	17.94	0.75	4.848	1.280	6.700	7.654	2.064	27.0
12/10/2010	12.65	0.72	5.261	1.425	7.636	8.875	1.672	18.8

[a] Coordinated universal time.

The third solid curve in Fig. 9b shows the temperatures after application of the calculated adjustments of the absorptivity or emissivity parameters. The curve fits very well in general but shows a slightly increasing deviation at the end. This may be due to gradual changes in the FCA absorptivity and/or emissivity parameters under aging and/or temperature effects [17].

Figure 10a shows the locations of five additional thermistors over the sail membrane. Figure 10b illustrates the temperatures measured by thermistors 1, 3, and 5 as well as their average values during the mission. Also shown are the predicted temperatures of the RCD sail surfaces calculated from the RCD thermo-optical parameters by means of Eq. (16).

The predicted and actual temperatures match fairly well with average and maximum differences between the two curves of only 2.1 and 3.7°C, respectively. Also, it is of interest to note that the measurements of thermistor 3 are closest to the predicted temperatures. This is likely due to the fact that thermistor 3 is located in between two RCD strips.

The results of Figs. 9b and 10b clearly indicate that there are considerable differences between the measured temperatures of the different membrane elements (even at the same time in the mission). This is due to the differences in the thermo-optical parameters of the various membrane surface elements.

Finally, we point out that the results of Figs. 9b and 10b provide justification for our conclusion that the virtual sail model with its uniform temperature predictions throughout the membrane is not realistic. Therefore, the uniform virtual sail model should be discarded in IKAROS case.

C. Sail-Induced Thermal Accelerations

Figure 11 shows the total acceleration, in units of nanometers per second squared, induced by the TRP originating from the seven

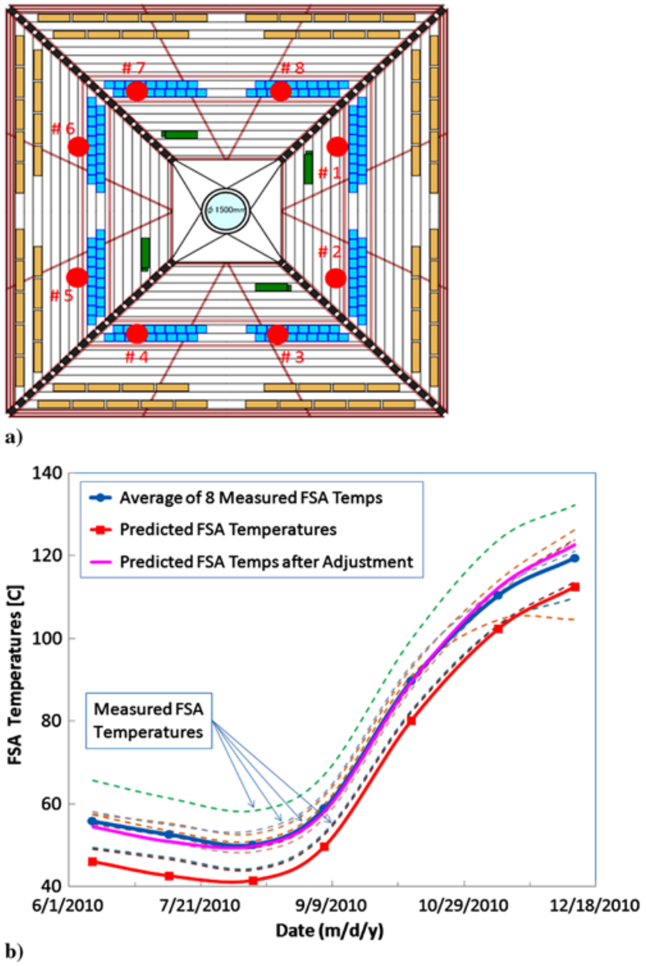

Fig. 9 Representations of a) locations of eight thermistors on flexible solar arrays, and b) measured and predicted temperatures in degrees Celsius.

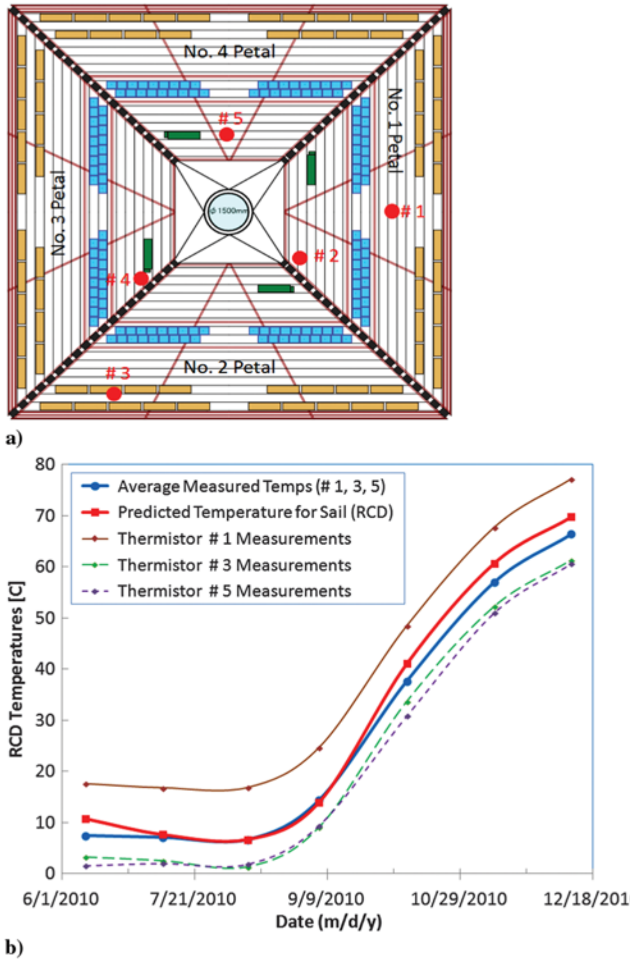

Fig. 10 Representations of a) locations of five thermistors on sail, and b) measured and predicted sail membrane temperatures in degrees Celsius.

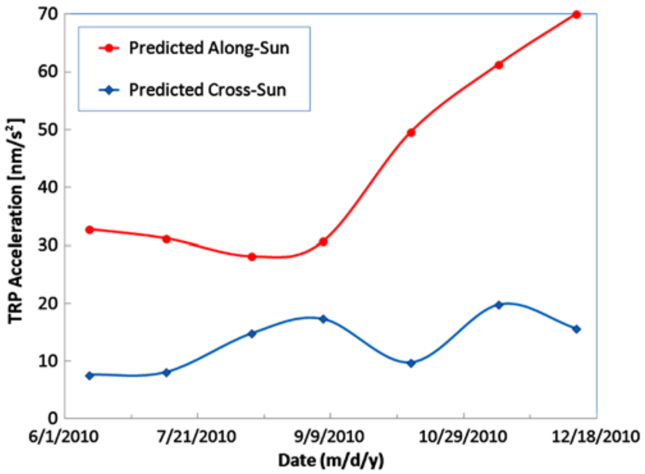

Fig. 11 Predicted TRP-induced acceleration components from all sail elements.

elements of the sail membrane based on the predictions in Eqs. (18–21). The acceleration is expanded in components along and normal to the sun direction. The former is in average almost 3.3 times larger than the latter. It should be noted that the direction of the TRP acceleration is directed toward the sun, which is opposite of the SRP force direction. This is because the overall recoil on the rear side of the sail dominates that on the front side by a factor of about 1.3.

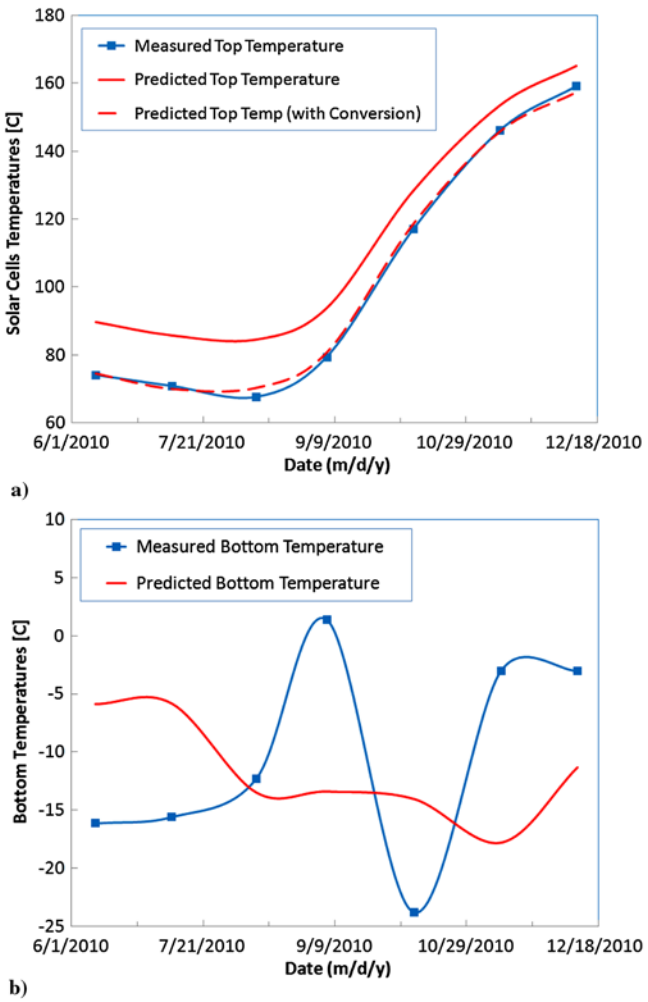

Fig. 12 Representations of a) measured and predicted temperatures for body top surface, and b) measured and predicted temperatures for body bottom surface.

The comparison of the results in Fig. 11 with the SRP-induced accelerations in Fig. 8 shows that they look qualitatively very similar. This is due to the fact that both effects depend on the solar aspect angle as well as solar distance, although in different ways.

In terms of their magnitudes, however, the acceleration due to the TRP effect is much smaller than the one induced by the SRP. Specifically, the along-sun TRP components are 0.8%, and the cross-sun components are about 1% of the respective SRP results in Fig. 8. Therefore, the TRP-induced accelerations from the sail are negligible in comparison with the SRP effects. In fact, already the in-flight variations of the SRP effects induced by the imperfections of a nonflat sail surface and due to variations of its optical properties would dominate over the thermal effects; see [6–8].

D. Body Front and Rear Temperatures

Figure 12a compares the predicted and measured temperatures of the IKAROS body top surface, which is covered by solar cells and optical reflectors. Two predictions are shown; the first one does not consider the power conversion in the solar cells, and the second one does account for the power conversion on the basis of the in-flight telemetry data. Figure 12a confirms that the temperature predictions that include the conversion effect are extremely accurate throughout the mission. The average value of the differences between predicted and in-flight measured temperatures is only about 0.5°C. If the power conversion effects are not taken into account, the average difference increases to 12.3°C.

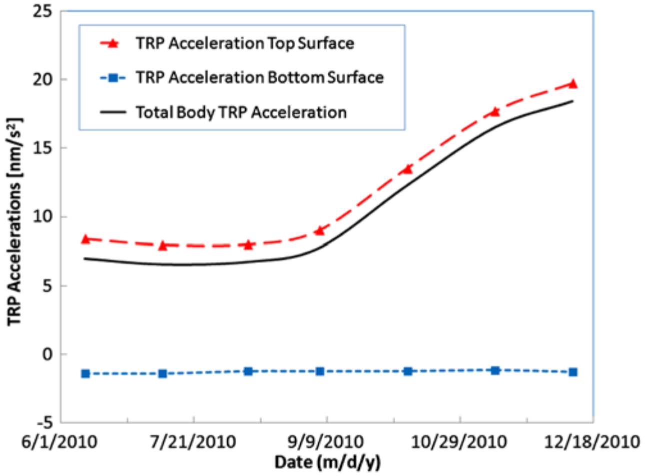

Fig. 13 TRP accelerations due to body surfaces.

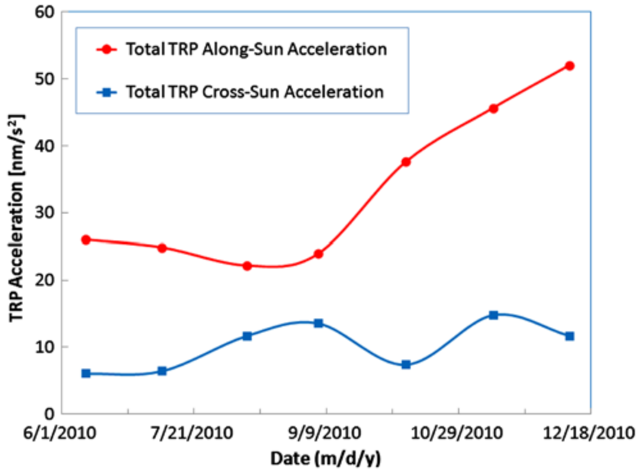

Fig. 14 Total TRP acceleration components induced by sail and body.

Table 4 Summary of temperatures and accelerations induced by thermal radiation pressure

		Measured temperatures, °C		Accelerations, nm/s^2			
Date[a]	Power conversion, W	Body top	Body bottom	Along $\boldsymbol{n}$	Along-sun	Cross-sun	Cross/along, %
6/10/2010	213.2	74.0	−16.1	26.7	26.0	6.05	23
7/9/2010	213.4	70.8	−15.6	25.7	24.9	6.42	26
8/10/2010	192.0	67.5	−12.3	25.1	22.2	11.7	53
9/6/2010	192.2	79.4	1.37	27.5	23.9	13.5	56
10/9/2010	190.5	117.1	−23.8	38.3	37.6	7.39	20
11/11/2010	180.7	146.3	−3.00	47.9	45.6	14.8	32
12/10/2010	197.8	159.2	−3.00	53.3	52.0	11.7	23

[a] Universal mean time.

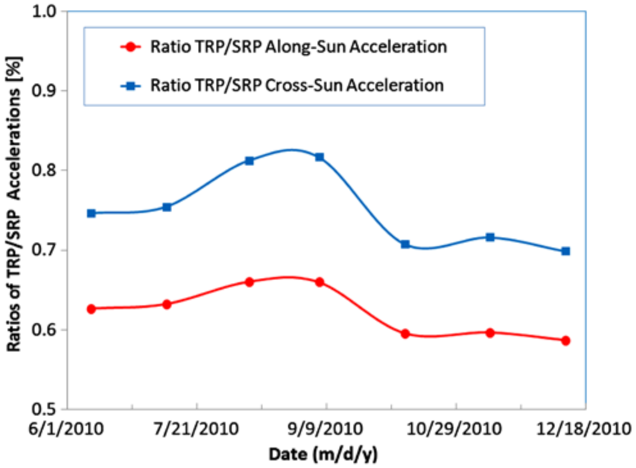

Fig. 15 Ratios of total TRP vs SRP along-sun and cross-sun acceleration components.

Figure 12b shows the predicted and observed in-flight temperatures of the bottom surface. The differences appear to be much larger than in Fig. 12a, especially at the peaks. However, the scale is different here, and the average difference between these temperatures is only 1.4°C. When comparing Fig. 12b with Fig. 7, we see that the differences between measured and predicted temperatures appear to be positively correlated with the solar aspect angle. It is possible that the solar energy that enters the body's interior through the MLI sheets on the body's side and bottom surfaces (see Fig. 5a) increases for higher solar aspect angles. This in turn will lead to higher temperatures on the bottom surface.

E. Body-Induced and Total Thermal Accelerations

Figure 13 shows the accelerations due to the TRP effects originating from the body's top and bottom surfaces, which have opposite signs. The magnitude of the acceleration from the top surface is in average close to 10 times that of the acceleration induced by the bottom surface. Thus, the total effective body TRP acceleration remains close to the contribution of the top surface, as shown in Fig. 13.

Figure 14 shows the total TRP-induced accelerations on IKAROS due to the membrane and body surfaces in their components along and normal to the spacecraft-sun direction. It should be noted that the TRP effect from the body front surface points away from the sun direction and thus acts opposite to the TRP acceleration from the sail surfaces. Therefore, the magnitudes of the accelerations in Fig. 14 are reduced relative to those originating from the sail on its own; see Fig. 11.

Table 4 gives the power conversion data and summarizes the results for the temperatures and TRP-induced accelerations. The trajectory perturbations due to the thermal radiation pressure are up to about 1% of the SRP. Therefore, they may be neglected in view of the considerable uncertainties in the solar radiation force model as mentioned previously; see also [6–8].

F. Ratios of Total Thermal and Thermal-Radiation-Pressure-Induced Accelerations

Finally, Fig. 15 shows the percentage ratios of the total acceleration components induced by the TRP and the SRP effects for the along-sun as well as the cross-sun directions. These results indicate that both of these ratios stay within the range from 0.5 to 0.9% and that the cross-sun ratio is always about 0.12% larger than the along-sun ratio. The maxima of these ratios occur in late August 2010 and coincide with the interval of maximum solar aspect angles shown in Fig. 7.

VI. Conclusions

The paper presents a detailed model and evaluation for the solar and thermal radiation accelerations acting on the IKAROS solar sail membrane and spacecraft body during its half-year operational mission from June to December 2010. In particular, comparisons are made between the predicted temperatures and the actual in-flight temperature readings delivered by thermistors located on the membrane and on the spacecraft body. When accounting for solar power conversion, the results show excellent correspondence for the body's top surface, which is covered by solar cells. On the other hand, appreciable differences have been observed for a few of the thermistors on the solar sail membrane. In any case, the temperature variations over the different sail membrane elements are significant because of the differences in thermo-optical parameters. As a consequence, a model considering a virtual sail with uniformly constant temperatures is not realistic. The results confirm that the trajectory perturbations induced by the thermal radiation pressure remain below 1% of the solar radiation effect. Therefore, they may be neglected in view of other error sources that may affect the solar radiation force, like for instance the effects of a nonflat sail and variations of its optical properties with temperature and lifetime.

References

[1] Kawaguchi, J., Mimasu, Y., Mori, O., Funase, R., Yamamoto, T., and Tsuda, Y., "IKAROS—Ready for Lift-Off as the World's First Solar Sail Demonstration in Interplanetary Space," *Proceedings of the 60th International Astronautical Congress of the International Astronautical Federation*, IAC Paper 09-D1.1.3, Daejeon, Republic of Korea, Oct. 2009.

[2] Mori, O., Sawada, H., Funase, R., Morimoto, M., Endo, T., Yamamoto, T., Tsuda, Y., Kawakatsu, Y., and Kawaguchi, J., "First Solar Power Sail Demonstration by IKAROS," *Proceedings of the 27th International Symposium on Space Technology and Science of the Japan Society for Aeronautical and Space Sciences*, ISTS Paper 2009-o-4-07v, Tsukuba, Japan, July 2009.

[3] Mimasu, Y., van der Ha, J. C., Yamaguchi, T., Funase, R., Tsuda, Y., Mori, O., and Kawaguchi, J., "Estimation of Solar Radiation Pressure Parameters for Solar Sail Demonstrator IKAROS Considering Attitude Dynamics," *Advances in the Astronautical Sciences*, Vol. 136, edited by Mortari, D., Starchville, T. F., Jr., Trask, A. J., and Miller, J. K., Univelt, San Diego, CA, 2010, pp. 1915–1932.

[4] Funase, R., Shirasawa, Y., Mimasu, Y., Mori, O., Tsuda, Y., Saiki, T., and Kawaguchi, J., "On-Orbit Verification of Fuel-Free Attitude Control System for Spinning Solar Sail Utilizing Solar Radiation Pressure," *Advances in Space Research*, Vol. 48, No. 11, 2011, pp. 1740–1746. doi:10.1016/j.asr.2011.02.022

[5] Mimasu, Y., Yamaguchi, T., Matsumoto, M., Nakamiya, M., Funase, R., and Kawaguchi, J., "Spinning Solar Sail Orbit Steering via Spin Rate

Control," *Advances in Space Research*, Vol. 48, No. 11, 2011, pp. 1810–1821.
doi:10.1016/j.asr.2011.08.030

[6] Tsuda, Y., Mori, O., Funase, R., Sawada, H., Yamamoto, T., Saiki, T., Endo, T., and Kawaguchi, J., "Flight Status of IKAROS Deep Space Solar Sail Demonstrator," *Acta Astronautica*, Vol. 69, Nos. 9–10, Nov.–Dec. 2011, pp. 833–840.
doi:10.1016/j.actaastro.2011.06.005

[7] Tsuda, Y., Saiki, T., Funase, R., and Mimasu, Y., "Generalized Attitude Model for Spinning Solar Sail Spacecraft," *Journal of Guidance, Control and Dynamics*, Vol. 36, No. 4, July–Aug. 2013, pp. 967–974.
doi:10.2514/1.59516

[8] Yamaguchi, T., Mimasu, Y., Tsuda, Y., and Yoshikawa, M., "Hybrid Estimation of Solar Radiation Pressure for a Spinning Solar Sail Spacecraft," *Journal of Spacecraft and Rockets*, Vol. 51, No. 1, Jan.–Feb. 2014, pp. 381–384.
doi:10.2514/1.A32387

[9] Shoemaker, M., van der Ha, J. C., and Morley, T., "Modeling and Validation of Thermal Radiation Acceleration on Interplanetary Spacecraft," *Journal of Spacecraft and Rockets*, Vol. 49, No. 2, March–April 2012, pp. 212–219.
doi:10.2514/1.A32063

[10] van der Ha, J. C., and Stramaccioni, D., "Thermal Radiation Effects on Deep Space Trajectories," *Spaceflight Mechanics 2010*, Vol. 136, Advances in the Astronautical Sciences, edited by Mortari, D., Starchville, T. F., Jr., Trask, A. J., and Miller, J. K., Univelt, San Diego, CA, 2010, pp. 1861–1880.

[11] van der Ha, J. C., "Model for Thermal Radiation Recoil Accelerations of Interplanetary Satellites," *Proceedings of the 28th International Symposium on Space Technology and Science of the Japan Society for Aeronautical and Space Sciences*, ISTS Paper 2011-d-55, Ginowan, Japan, June 2011.

[12] Sugimoto, Y., and van der Ha, J. C., "Thermal Radiation Modeling for Interplanetary Spacecraft Orbit Propagation," *28th International Symposium on Space Technology and Science of the Japan Society for Aeronautical and Space Sciences*, ISTS Paper 2011-d-57, Ginowan, Japan, June 2011.

[13] Kato, T., and van der Ha, J. C., "Precise Modeling of Solar and Thermal Accelerations on Rosetta," *Acta Astronautica*, Vol. 72, No. 2, March 2012, pp. 165–177.
doi:10.1016/j.actaastro.2011.09.009

[14] Rievers, B., Kato, T., van der Ha, J. C., and Laemmerzahl, C., "Numerical Prediction of Satellite Surface Forces with Application to Rosetta," *Space Flight Mechanics 2012*, Vol. 143, Advances in the Astronautical Sciences, edited by McAdams, J. V., McKinley, D. P., Berry, M. M., and Jenkins, K. L., Univelt, San Diego, CA, 2012, pp. 1123–1142.

[15] Kato, T., Rievers, B., van der Ha, J. C., and Laemmerzahl, C., "Sensitivity Analysis of the Non-Gravitational Perturbations on Mercury Orbiter," *Space Flight Mechanics 2012*, Vol. 143, Advances in the Astronautical Sciences, edited by McAdams, J. V., McKinley, D. P., Berry, M. M., and Jenkins, K. L., Univelt, San Diego, CA, 2012, pp. 1579–1595.

[16] van der Ha, J. C., "Comparison of Solar and Thermal Radiation Accelerations of Deep-Space Satellites," *Space Flight Mechanics 2014*, Vol. 152, Advances in the Astronautical Sciences, edited by Mackison, D., Wilson, R., Abdelkhalik, O., and Zanetti, R., Univelt, San Diego, CA, 2014, pp. 2727–2746.

[17] Pisacane, V. L., *The Space Environment and Its Effects on Space Systems*, AIAA Education Series, AIAA, Reston, VA, 2008, p. 70.

R. Sedwick
Associate Editor